Chemical Science

Accepted Manuscript

This article can be cited before page numbers have been issued, to do this please use: X. Ma, E. Xie, Q. Li, C. Sun, Y. Yao, C. Yan, Q. Luo, Z. Guo and W. Zhu, *Chem. Sci.*, 2026, DOI: 10.1039/D6SC02037B.

ROYAL SOCIETY OF CHEMISTRY

rsc.li/chemical-science

View Article Online
DOI: 10.1039/D6SC02037B

ARTICLE

Charge-regulated hepatic *γ*-glutamyltranspeptidase fluorescent probe: *in vivo* staging *Schistosoma*-infection

Received 00th January 20xx,
Accepted 00th January 20xx

DOI: 10.1039/x0xx00000x

Xiaoxi Ma[a], Eryang Xie[a], Qiang Li[c], Chuyang Sun[a], Yongkang Yao[a], Chenxu Yan*[,a], Qianfu Luo*[,a], Zhiqian Guo*[,a,b] & Wei-Hong Zhu[a]

Schistosomiasis remains a formidable global health threat, yet current diagnostic modalities like microscopy and ultrasonography suffer from limited sensitivity and critical inability for real-time *in vivo* monitoring, posing significant hurdles in precise infection staging. To address this diagnostic bottleneck, we develop a *de novo* strategic charge-regulation approach for developing a dual-channel near-infrared fluorescent probe toward hepatic *γ*-glutamyltranspeptidase (GGT), a key biomarker for schistosomiasis-induced liver pathological evolution. By engineering quinoline scaffold from zwitterionic, single positive charge, to double positive charge, the optimized probe QMC-N-GGT achieves superior precise targeting to the infected liver tissues with anionic microenvironment. Impressively, its dual-channel signals make a breakthrough to track when, where, and how the probe targets the liver and *in situ* lights up endogenous GGT. This probe exhibits a remarkable stage-dependent fluorescent response to GGT, enabling accurate distinction of slight, middle, and severe infection stages with an ultra-high signal-to-noise ratio. QMC-N-GGT thus represents an unprecedented diagnostic tool, bridging the gap between conventional infection screening and advanced pathological staging for non-invasive, real-time schistosomiasis monitoring.

INTRODUCTION

Schistosomiasis, caused by trematode flukes of the genus *Schistosoma*, is the second most prevalent parasitic disease worldwide.[1-4] Triggered by tissue-trapped eggs, schistosomiasis leads to serious pathologies ranging from systemic symptoms to multi-organ damage, such as severe hepatosplenism, progressive fibrosis, and so on.[5-7] Three distinct phases exist in schistosomiasis progression (acute infection, established active infection, and late chronic infection), each stage requiring specific therapeutic interventions.[8,9] As such, real-time staging and evolution identification of *Schistosoma*-infection are essential for clinical management. However, a fundamental challenge is how to non-invasively assess these dynamic staging processes *in vivo*. Current approaches harness *in vitro* detection (Fig. 1A), relying on microscopic counting of viable eggs in urine, faeces, or tissue biopsies. Owing to the limited sensitivity, the presence of infecting schistosomes cannot be ruled out definitively. As for *in vivo* diagnosis, ultrasonography is generally confined to detecting pathological changes in the late stages of infection. Consequently, a tool that could identify the spatiotemporal progression across stages, would have critical utility in the clinical management of schistosome-induced conditions.

Fluorescence-based technologies[10-14] have revolutionized the *in vivo* monitoring of biomarkers.[15-19] Especially for schistosomiasis, *γ*-glutamyltransferase (GGT) has emerged as a crucial enzymatic marker,[20-22] as it's markedly upregulated during schistosomiasis-induced hepatic granuloma formation and subsequent fibrosis,[2,23,24] with its catalytic activity showing a strong positive correlation with the infectious progression.[25-27] As such, developing activatable probes to track hepatic GGT activity presents an effective strategy for the real-time staging of schistosomiasis.[28-30] However, the intrinsic pathological complexity of *Schistosoma*-infection, characterized by deep-tissue hepatic sequestration and dynamic evolution features, poses significant hurdles for probe design.[31-35] In this regard, we reasoned that two prerequisites are essential: one is to modulate the charge properties of the molecular scaffold to optimize pharmacokinetics for hepatotropic enrichment;[36-40] the other is to incorporate an additional emission channel to transform conventional "turn-on" probes into dual-channel ratiometric sensors, enabling high-fidelity identification of GGT activity *in situ* and *in vivo*.

[a]*Key Laboratory for Advanced Materials and Institute of Fine Chemicals, Feringa Nobel Prize Scientist Joint Research Center, Frontiers Science Center for Materiobiology and Dynamic Chemistry, School of Chemistry and Molecular Engineering, East China University of Science and Technology, Shanghai 200237, China. E-mail: chenxuyan@ecust.edu.cn; luogf@ecust.edu.cn; guozq@ecust.edu.cn*
[b]*State Key Laboratory of Bioreactor Engineering, East China University of Science and Technology, Shanghai 200237, China.*
[c]*National Key Laboratory of Intelligent Tracking and Forecasting for Infectious Diseases, National Institute of Parasitic Diseases at Chinese Center for Disease Control and Prevention, Chinese Center for Tropical Diseases Research, National Research Center for Tropical Diseases, Key Laboratory of Parasite and Vector Biology, National Health Commission, WHO Collaborating Center for Tropical Diseases, National Center for International Research on Tropical Diseases, Ministry of Science and Technology, Shanghai 20025, China.*

Electronic Supplementary Information (ESI) available: [details of any supplementary information available should be included here]. See DOI: 10.1039/x0xx00000x

View Article Online
DOI: 10.1039/D6SC02037B

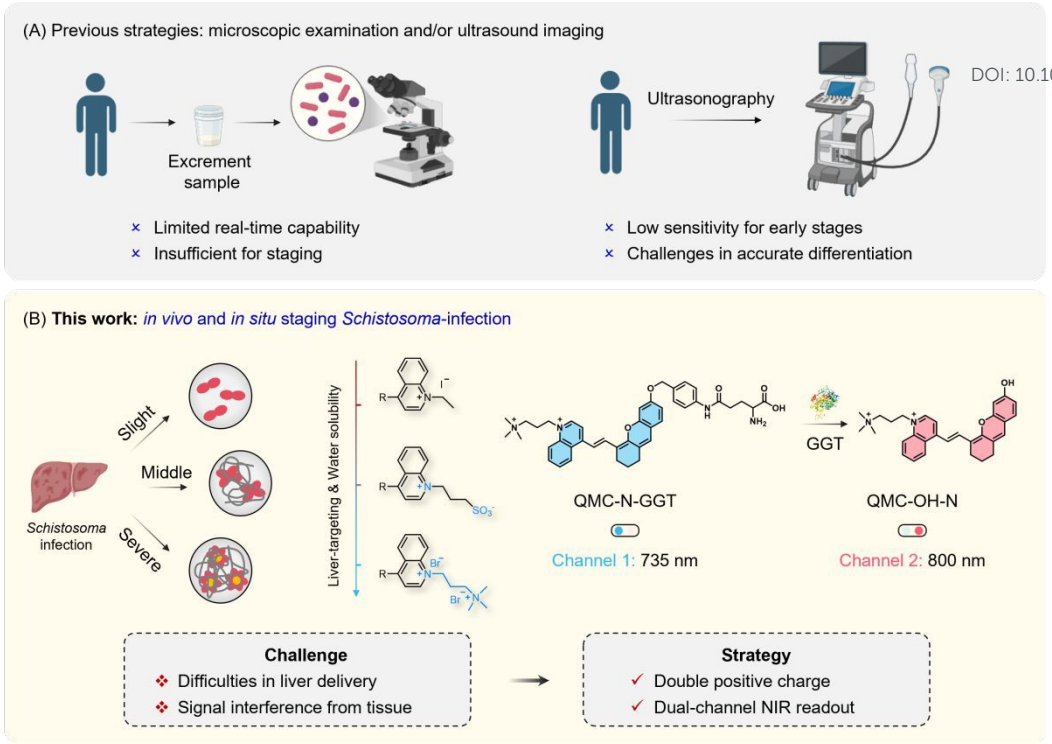

Fig. 1. Double positive charged NIR fluorescent probe: dual-channel mapping liver γ-glutamyltranspeptidase for staging *Schistosoma*-infection. (A) Limitations of current diagnostics for staging *Schistosoma*-infection. (B) Double positive charged NIR probe for dual-channel mapping hepatic *γ*-glutamyltransferase (GGT), enabling the intact *in vivo* staging of schistosomiasis progression.

Herein, we present a charge-regulated dual-channel NIR probe strategy to address the limitations of traditional microscopic examination and ultrasonography in schistosomiasis monitoring. This strategy centers on a quinoline scaffold, featuring precisely tailored charged centers[41-44] (from zwitterionic, single positive charge, to double positive charge) that optimize pharmacokinetic behavior for hepatotropic enrichment and retention (Fig. 1B). Our optimized probe, QMC-N-GGT, integrates a dicationic core to significantly enhance systemic circulation and liver targeting capability via electrostatic attraction to the anionic microenvironment of damaged liver tissues. Crucially, its dual-channel ratiometric signaling provides real-time feedback to track when, where, and how the probe targets the liver and *in situ* lights up endogenous GGT. *In vivo* imaging results provide solid evidence that QMC-N-GGT could differentiate markedly among severity evolution (including slight, middle, and severe infection stages) via both the fluorescent response kinetics and intensity. This integrated approach offers an intact molecular imaging platform for the high-fidelity *in vivo* staging of schistosomiasis, representing a potent chemical tool for multiscale assessment of infection dynamics.

RESULTS AND DISCUSSIONS

Double positive charged quinoline NIR fluorophore with hepatic targeting and retention

Given that the pathogenesis of schistosomiasis is characterized by the formation of spatially heterogeneous hepatic fibrosis, an effective imaging agent must meet two key criteria: efficient liver accumulation to target infection sites and NIR fluorescence to ensure sufficient penetration for deep liver imaging. To address these requirements, we selected quinoline as the fluorophore building block due to its inherent sensitivity to electronic modifications and tunable intramolecular charge transfer (ICT) characteristics. As established, the major components of the liver extracellular matrix (ECM) include glycoproteins and negatively charged proteoglycans, such as chondroitin sulfate, biglycan, and decorin. In fibrotic liver, the ECM components are similar to those in normal liver but are quantitatively increased, leading to an increase in overall negative charge.[45,46] As such, we reasoned charge-regulation approach could improve the probe's hepatic targeting and retention. With this in mind, we designed and synthesized a series of quinoline-based candidates with distinct electronic properties (Fig. 2A): QMC-OH-C (single positive charged), QMC-OH-SO_3 (zwitterionic), and QMC-OH-N (double positive charged). As expected, all derivatives exhibit typical NIR properties, with absorption and emission maxima centered at around 580 nm and 735 nm, respectively (Fig. 2B and 2C). Then, we examined how charge characteristics serve as a key determinant of the fluorophores' water solubility and pharmacokinetic behavior.

To assess the water solubility, we conduct the test of concentration-dependent absorbance spectra. As shown in Fig. 2D and S1, QMC-OH-N maintains a consistently higher absorbance than QMC-OH-C across the tested concentration range, indicating much better miscibility of QMC-OH-N. These results strongly support that double positive charge regulation substantially enhances aqueous solubility and effectively suppresses nonspecific aggregation in aqueous media. We next investigated the pH-dependent spectral behavior of QMC-OH-N. As pH increased from 5.0 to 10.0, the pH-dependent absorption spectra exhibited a clear bathochromic shift

View Article Online
DOI: 10.1039/D6SC02037B

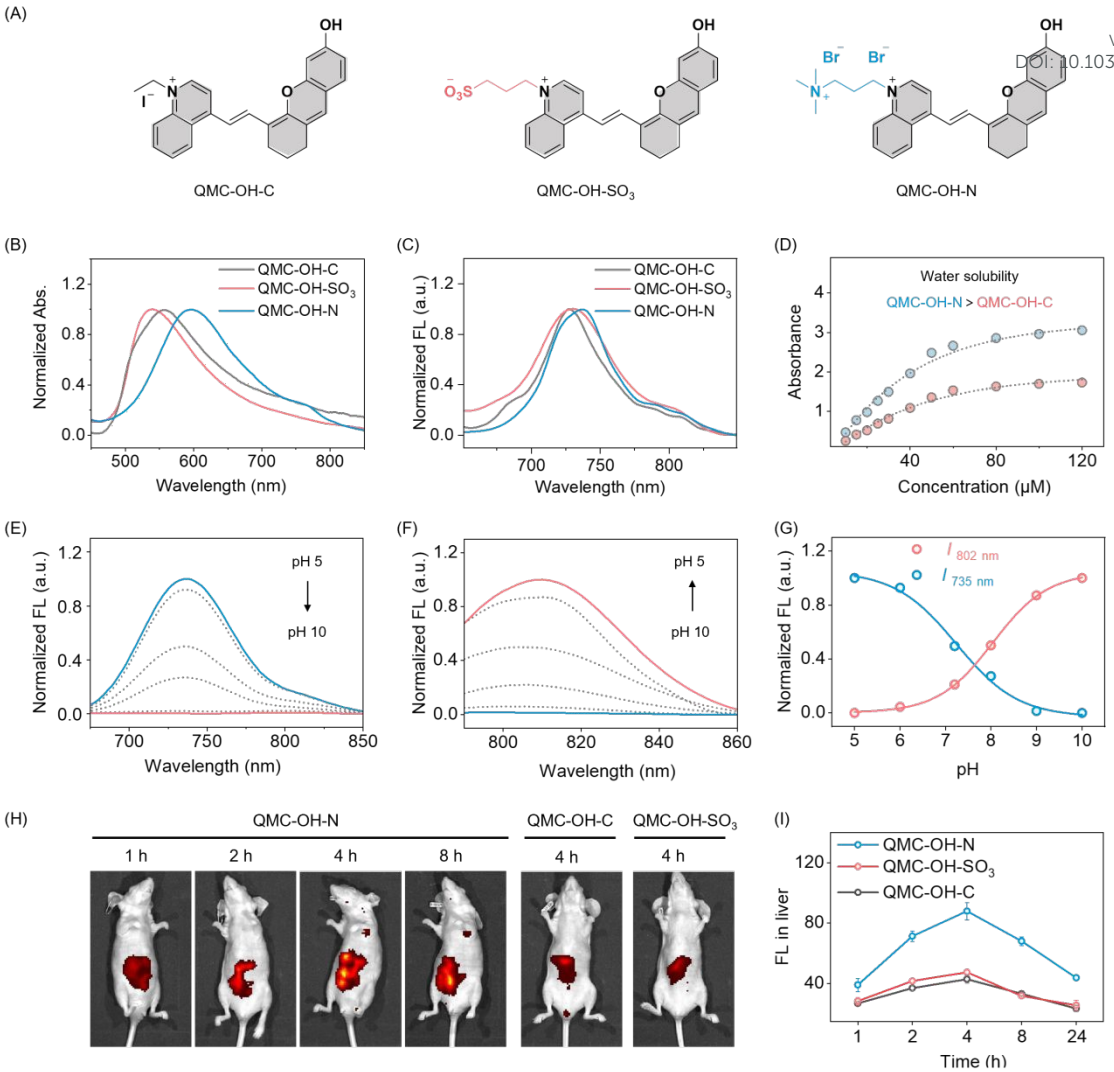

Fig. 2 Charge-modulated quinoline NIR fluorophores with good miscibility and liver targeting. (A) Chemical structures of three tailored NIR fluorescent probes: QMC-OH-C, QMC-OH-SO_3, and QMC-OH-N. (B and C) Normalized absorption (B) and fluorescence (C) spectra of the QMC dyes in aqueous solution, exhibiting characteristic NIR emission centered at approximately 735 nm (λ_{ex} = 620 nm, 10 μM). (D) Comparative water solubility evaluation. The concentration-dependent absorbance plots highlight the superior linear dynamic range and improved dispersity of the cationic QMC-OH-N compared to the anionic QMC-OH-C. (E and F) pH-dependent fluorescence response of QMC-OH-N (10 μM, pH 5.0 to 10.0, λ_{ex} = 620 nm). (G) Ratiometric pH titration curves based on the fluorescence intensity ratio. (H) Representative real-time NIR fluorescence images of healthy mice at different time intervals (1, 2, 4, and 8 h) after intravenous injection of QMC-OH-C, QMC-OH-SO_3, and QMC-OH-N. (I) Time-dependent fluorescence intensity profiles in the liver region of mice (n = 3). Data are expressed as mean ± s.d.

in the maximum absorption wavelength (Fig. S2, from 620 nm to 760 nm). Simultaneously, we observed a substantial decrease in fluorescence intensity at 735 nm (Channel 1, λ_{ex} = 620 nm), accompanied by a sharp enhancement of a new NIR emission band centered at 800 nm (Channel 2, λ_{ex} = 760 nm, Fig. 2E-2G). As shown in Fig. S3, the pK_a constant of the probe was determined to be 5.5, confirming that QMC-OH-N remains in its stable sensing state under physiological conditions. This spectral evolution is attributed to the deprotonation of the phenolic hydroxyl group, which transforms the zwitterionic hydroxyl donor into a potent phenolate anion, thereby strengthening the ICT effect within the quinoline scaffold and causing the observed bathochromic shift both in absorption and emission. This dual-channel NIR strategy offers a robust molecular imaging platform, serving as a potent chemical tool for the assessment of infection dynamics.

We then evaluated the *in vivo* pharmacokinetic and liver targeting efficiency of the quinoline dyes. Following intravenous injection, QMC-OH-N demonstrated superior liver enrichment and prolonged retention compared to QMC-OH-C and QMC-OH-SO_3 (Fig. 2H). Quantitative analysis of the liver fluorescence showed that QMC-OH-N reached peak intensity at 4 hours post-injection, with a signal approximately 2-fold higher than the other two candidates (Fig. 2I). This significantly enhanced liver targeting capability is mainly attributed to the electrostatic attraction toward the anionic microenvironment (rich in glycosaminoglycans and proteoglycans) of liver tissues. All these spectral and pharmacokinetic results highlight that the dicationic QMC-OH-N exhibits good water solubility,

View Article Online
DOI: 10.1039/D6SC02037B

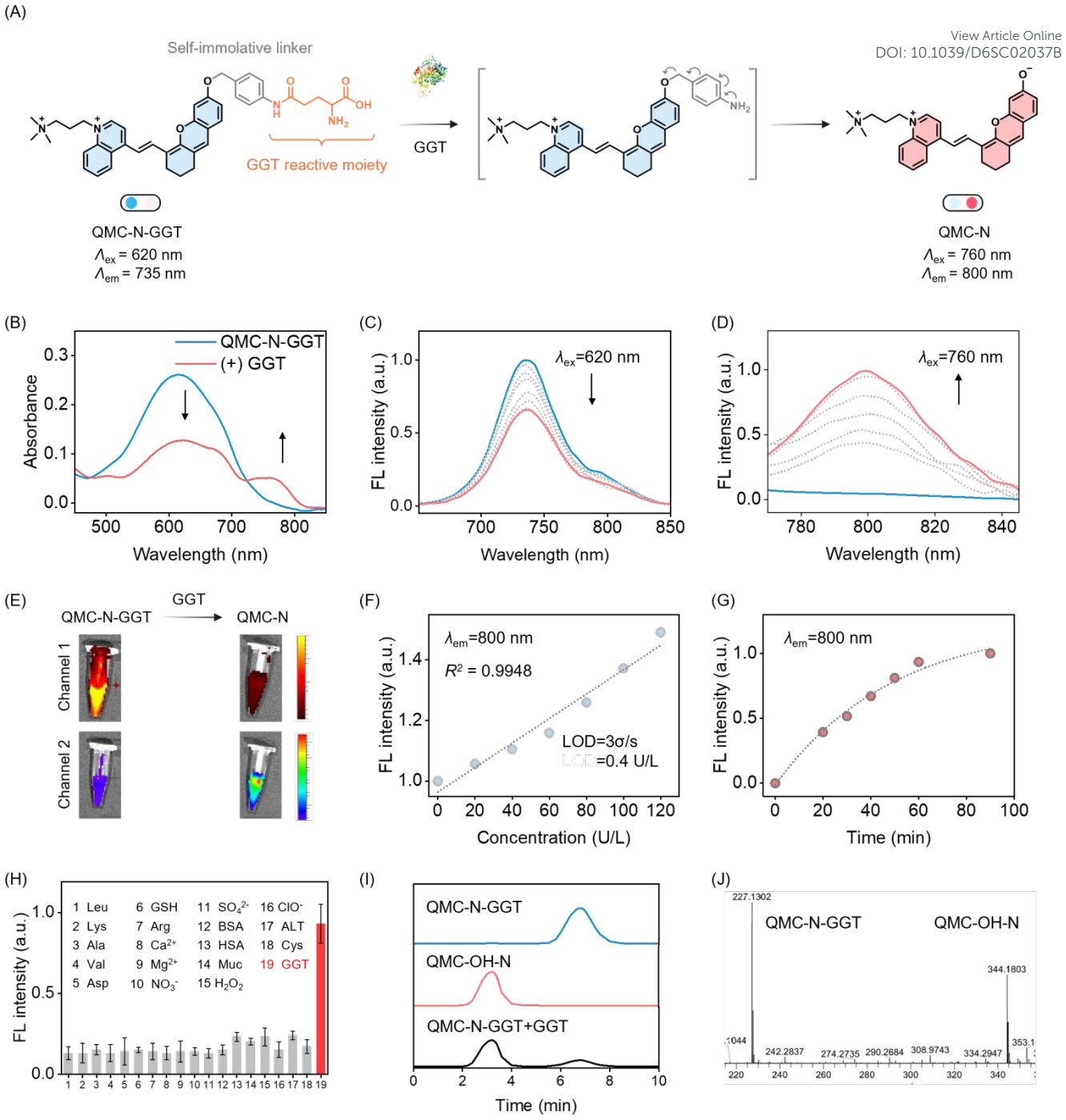

Fig. 3 High-fidelity sensing of GGT via dual-channel NIR fluorescence. (A) Schematic illustration of the probe design and the GGT-activated dual-channel fluorescence response. (B) Absorption spectra of QMC-N-GGT (10 μM) in the absence and presence of GGT (120 U L^{-1}). (C and D) Dual-channel NIR fluorescence responses of QMC-N-GGT (10 μM) upon incubation with GGT (120 U L^{-1}). Channel 1: λ_{ex} = 620 nm, λ_{em} = 735 nm (C); and Channel 2: λ_{ex} = 760 nm, λ_{em} = 800 nm. (E) Representative macroscopic imaging of QMC-N-GGT (10 μM) before and after GGT (120 U L^{-1}) activation across dual NIR channels (Channel 1: λ_{ex} = 620 nm, λ_{em} = 640-750 nm; Channel 2: λ_{ex} = 760 nm, λ_{em} = 770-850 nm). (F) Quantitative correlation between the fluorescence intensity at 800nm and GGT concentrations (0–120 U L^{-1}). (G) Kinetic profiles of the GGT-triggered fluorescence enhancement at 800 nm. (H) Sensing specificity of QMC-N-GGT (10 μM, λ_{ex} = 760 nm,

sensitive dual-channel NIR response,[47-52] excellent hepatic targeting and retention. We thus envisaged that conjugating a GGT-responsive moiety to this scaffold would yield a dual-channel NIR probe for the real-time *in vivo* monitoring of *Schistosoma*-infection.

GGT-triggered dual-channel NIR fluorescence

To implement our sensing strategy, we incorporated *γ*-glutamyl reactive moiety into the phenolic hydroxyl group of the three quinoline-based fluorophores, generating a series of dual-channel NIR probes toward GGT: QMC-C-GGT, QMC-SO_3-GGT, and QMC-N-GGT (Fig. 3A and S4). For instance of QMC-N-GGT,

View Article Online
DOI: 10.1039/D6SC02037B

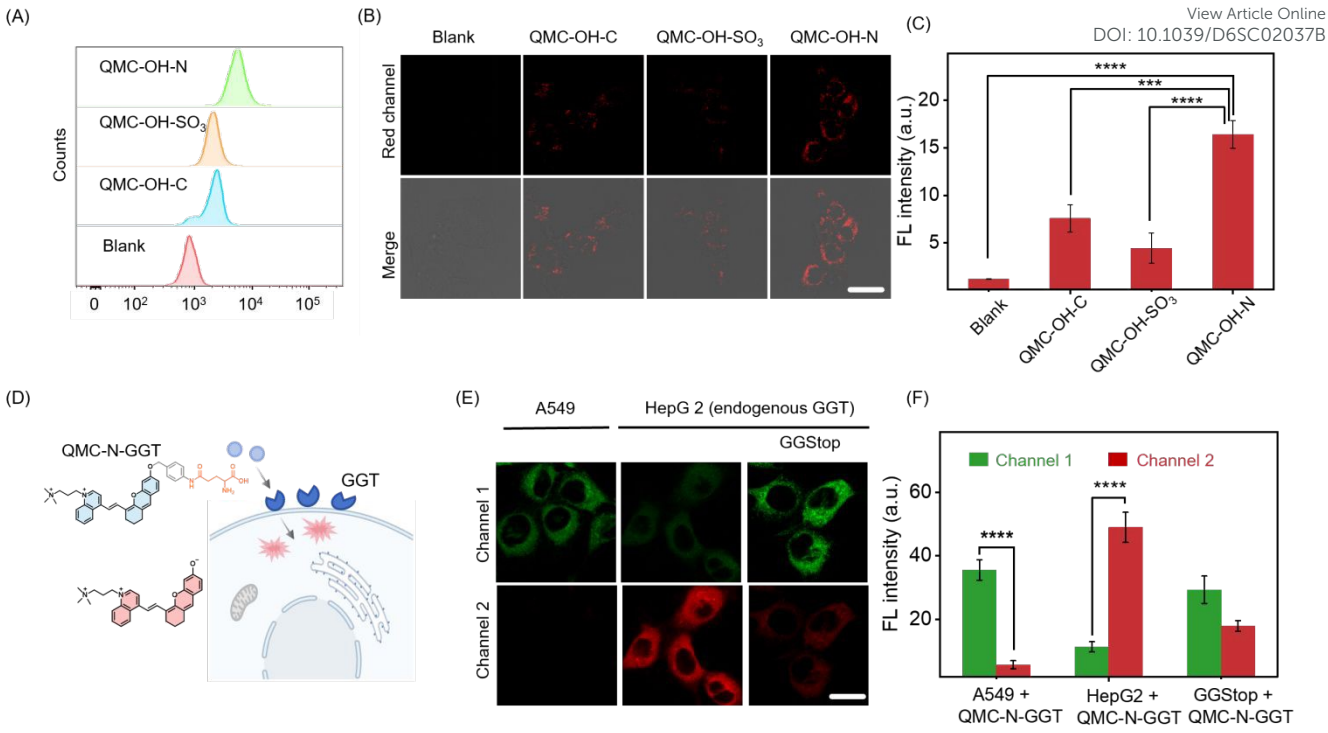

Fig. 4 Endogenous GGT-activatable fluorescence. (A) Flow cytometry analysis of HepG2 cells incubated with QMC-OH-C, QMC-OH-SO_3, and QMC-OH-N (10 μM). (B and C) Confocal laser scanning microscopy images (B) and corresponding mean fluorescence intensity (C) of HepG2 cells treated with the three probes (λ_{ex} = 620 nm, λ_{em} = 640-750 nm). Scale bar: 20 μm. ****P<0.0001 by unpaired two-tailed Student's t-test. (D and E) High-contrast imaging of endogenous GGT activity in different cell lines (QMC-OH-N 10 μM, Channel 1: λ_{ex} = 620 nm, λ_{em} = 640-750 nm; Channel 2: λ_{ex} = 760 nm, λ_{em} = 770-850 nm). Scale bar: 20 μm. (F) Quantitative fluorescence intensity of Channel 1 and Channel 2 across each group in panel E. ****P<0.0001.

the probe was specifically designed by conjugating a γ-glutamyl moiety to the QMC-OH-N scaffold via a *p*-aminobenzyl alcohol-based self-immolative linker. We then carefully evaluated the GGT-triggered spectral response of QMC-N-GGT. Initially, the probe exhibited a strong absorption peak at 620 nm (Fig. 3B). Upon the addition of GGT, a new absorption peak around 735 nm appeared. This spectral evolution is more obvious in the fluorescence spectra: upon addition of GGT, the fluorescence at 735 nm undergoes a substantial decrease (Channel 1, λ_{ex} = 620 nm), with a concomitant rise of a new NIR emission band peaking at 800 nm (Channel 2, λ_{ex} = 760 nm, Fig. 3C-3E). The fluorescence intensity of QMC-N-GGT at 800 nm exhibited a well-defined linear relationship with GGT concentration in the range of 0-120 U L^{-1}. The calculated LOD of 0.4 U L^{-1} is substantially lower than clinical GGT thresholds, validating the probe's exceptional capability for the sensitive monitoring of hepatic GGT activity.(Fig. 3F). Kinetic analysis revealed that the fluorescence intensity at 800 nm increased and then reached a plateau around 60 min (Fig. 3G). QMC-N-GGT also showed excellent GGT-specificity against various potential competitive species, including common amino acids, inorganic ions, and biological macromolecules as well as biologically relevant reactive oxygen species (ROS) and biothiols (Fig. 3H). To ensure the reliability of QMC-N-GGT for persistent bioimaging, we confirmed its superior photostability in comparison with the clinical NIR fluorophore ICG (Fig. S5). These results highlighted the sensitivity and selectivity of QMC-N-GGT with GGT-triggered dual-channel NIR fluorescence response.

To further validate the proposed sensing mechanism, we conducted a comprehensive analysis using high-performance liquid chromatography (HPLC) and mass spectrometry (MS). As shown in Fig. 3I, the QMC-N-GGT probe exhibited a single characteristic peak at a retention time of 6.8 min. Upon incubation with GGT, a distinct new peak emerged at 3.2 min, which precisely aligned with the retention time of the independently synthesized active fluorophore QMC-OH-N. The ESI-MS spectrum of QMC-N-GGT incubated with GGT for 60 min showed observed m/z of 227.1302 and 344.1803 (Fig. 3J, corresponding to the hypothesized product QMC-OH-N and the probe QMC-N-GGT. Taken together, the dual-channel NIR fluorescence of QMC-N-GGT made it possible to track ratiometrically when, where, and how the probe targets the liver (Channel 1) and *in situ* lights up endogenous GGT (Channel 2).

Dual-channel NIR fluorescence tracking of endogenous GGT in living cells

To investigate the capability of QMC-N-GGT for tracking endogenous GGT activity, we examined its dual-channel fluorescence responses in living cells. We first assess the cellular internalization of the fluorophore engineered with different charge properties. Flow cytometry analysis indicated that double positive charged QMC-OH-N exhibited a pronounced

View Article Online
DOI: 10.1039/D6SC02037B

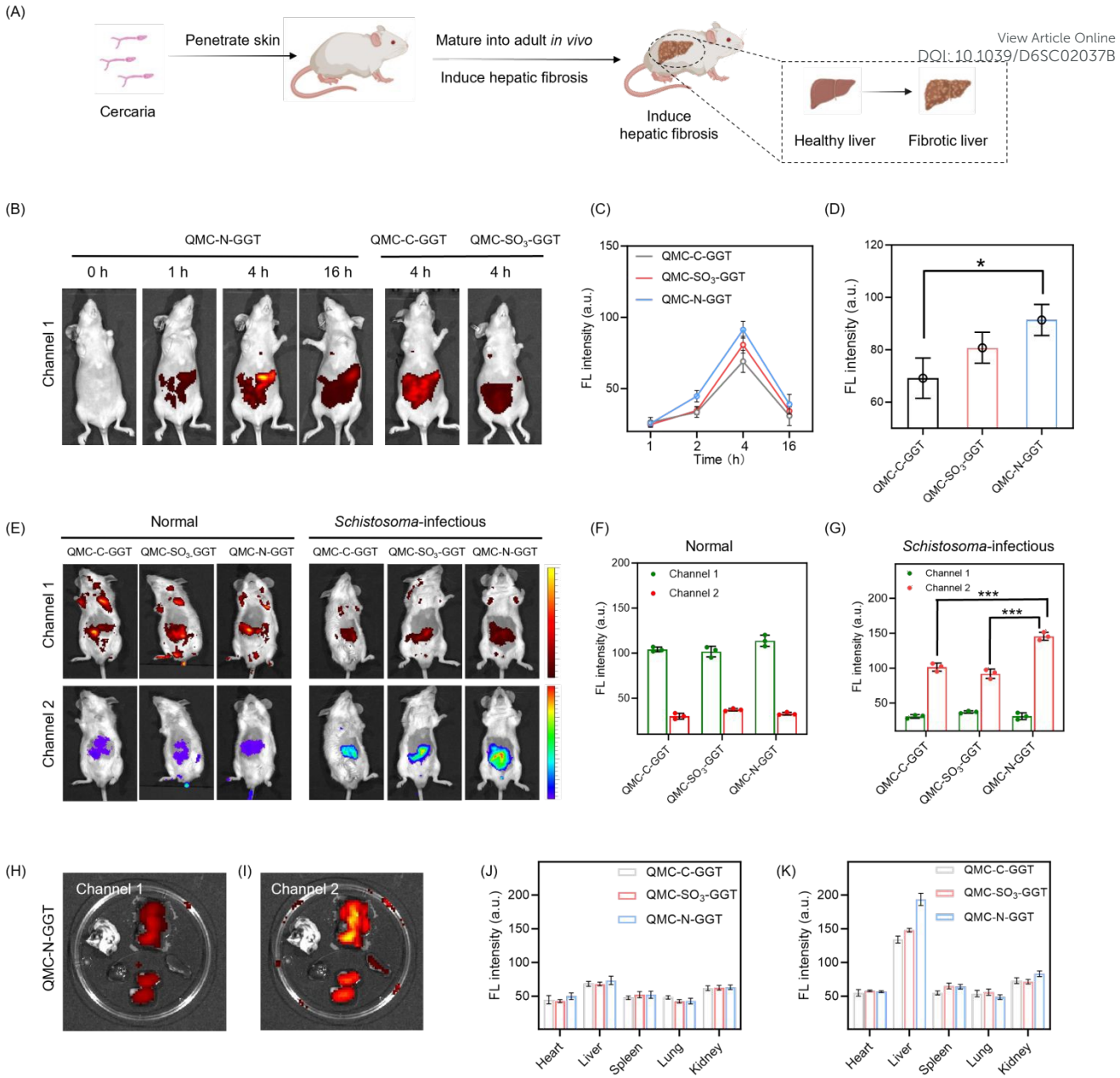

Fig. 5 Dual Channel GGT detection enabling *in vivo* mapping *Schistosoma*-infection. (A) Schematic illustration of the *Schistosoma*-infectious mouse model establishment. (B) *In vivo* NIR fluorescence imaging of healthy mice of the three probes (100 μM, Channel 1: λ_{ex} = 620 nm, λ_{em} = 640-750 nm). (C and D) Quantitative comparison of total fluorescence intensity (Channel 1) in the liver regions of healthy mice. ****P<0.0001 by unpaired two-tailed Student's t-test. (E) *In vivo* dual-channel NIR fluorescence imaging of healthy and infected mice one hour after intravenous injection of the three probes. (F and G) Statistical analysis of fluorescence signals in Channel 1 and Channel 2 for three probes in normal (F) and infectious (G) mice (100 μM, Channel 1: λ_{ex} = 620 nm, λ_{em} = 640-750 nm; Channel 2: λ_{ex} = 760 nm, λ_{em} = 770-850 nm). ****P<0.0001. (H and I) *Ex vivo* fluorescence images of major organs (heart, liver, spleen, lung, and kidney) in Channel 1 (H) and Channel 2 (I) at 24 h post-injection, confirming the specific activation in liver tissue. (J and K) Quantitative biodistribution (J, Channel 1) and activation analysis (J, Channel 2) in major organs for the three probes.

rightward shift in fluorescence counts compared to the zwitterionic alkyl-substituted QMC-OH-C and the anionic QMC-OH-SO_3 derivatives (Fig. 4A). This superior internalization was visually confirmed by confocal laser scanning microscopy, where QMC-OH-N-treated cells displayed the brightest and most uniform intracellular staining (Fig. 4B and 4C). Cytotoxicity assays in HepG2 and 293T cell lines confirmed that QMC-N-GGT exhibited negligible toxic effects (Fig. S6), demonstrating good biocompatibility for cellular sensing and imaging. Cell retention and co-localization assays further supported that the dicationic structure effectively prevents probe efflux through enhanced electrostatic interactions (Fig. S7 and S8).

View Article Online
DOI: 10.1039/D6SC02037B

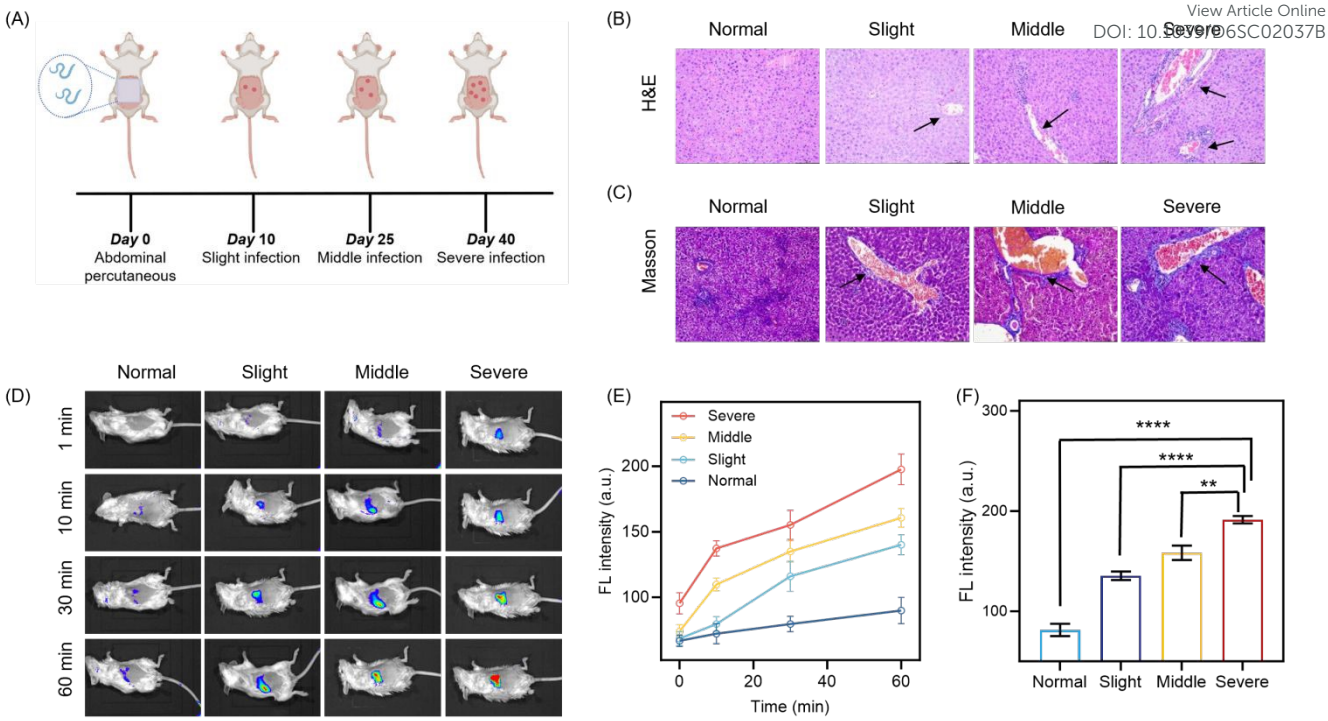

Fig. 6 Staging of *Schistosoma*-infection via NIR imaging. (A) Schematic illustration of the *Schistosoma*-infectious mouse model establishment, depicting the timeline from abdominal percutaneous infection (Day 0) to severe hepatic fibrosis (Day 40). (B and C) Representative histopathological images of liver sections from mice at distinct stages of *Schistosoma*-infection (normal, slight, middle, and severe). HE staining (B) shows normal hepatic tissue (pink) and an area of inflammatory lesions (purplish-blue). Tissue disruption due to the lesion is indicated by the black arrow. Masson's trichrome staining (C) shows normal liver tissue (pink) and areas of hepatic fibrosis (blue), with bridging fibrosis forming fibrous septa (black arrow). (D) Time-dependent *in vivo* NIR fluorescence imaging (1, 10, 30, and 60 min) of infectious mice following intravenous injection of QMC-N-GGT (100 μM, λ_{ex} = 760 nm, λ_{em} = 770-850 nm). (E) Kinetic plots of average fluorescence intensity at the liver site as a function of time (0–60 min) across the four groups, demonstrating stage-dependent activation rates. (E) Statistical comparison of the total fluorescence intensity at the liver site at 60 min post-injection, confirming the probe's ability to differentiate the severity of schistosomiasis. Data are expressed as mean ± s.d. (n = 3). ****P<0.0001 by unpaired two-tailed Student's t-test.

We next evaluate the intracellular sensing performance of the GGT-responsive probe QMC-N-GGT (Fig. 4D). In A549 cells (GGT-underexpressing cell line), fluorescence was observed primarily in Channel 1 (735 nm, Fig. 4E). In contrast, HepG2 cells (GGT-overexpressing)[53,54] showed a decrease in Channel 1 signal and a significant increase in Channel 2 emission (800 nm, Fig. 4E), confirming probe activation by the endogenous GGT. To further verify the specificity, we incubated HepG2 cells with GGStop (GGT inhibitor). As expected, this treatment suppressed the fluorescence increase at 800 nm, and the resulting signal levels correlated directly with cellular GGT activity (Fig. 4E and 4F). These results highlighted that QMC-N-GGT combined efficient cellular uptake, good biocompatibility, and specific dual-channel fluorescence response to endogenous GGT. Thus, QMC-N-GGT provides a reliable method for visualizing enzyme activity in living cells, and offers a promising tool for tracking GGT-relevant biological processes especially for *Schistosoma*-infection.

Double positive charge strategy enabling *in situ* identification of *Schistosoma*-infection via illuminating hepatic GGT

Based on the promising cellular GGT imaging performance, we then assessed the potential of QMC-N-GGT for *in vivo* identification of *Schistosoma*-infection via probing hepatic GGT. The pathology of schistosomiasis is characterized by the maturation of cercariae into adults, which triggers an intense inflammatory cascade and subsequent aberrant GGT upregulation during hepatic fibrosis. To model this, mice were percutaneously infected with cercariae following standardized protocols, leading to significant hepatic architectural remodeling (Fig. 5A).

We then investigated *in vivo* imaging performance by comparing the three charge-tailored probes (QMC-C-GGT, QMC-SO_3-GGT, and QMC-N-GGT) in both healthy and infected mice following intravenous injection. The distribution and activation of each probe were tracked via channel 1 (yellow-red) and 2 (rainbow) fluorescence readouts, respectively (Fig. 5B-5G). In healthy mice, the hepatic fluorescence intensity of QMC-N-GGT progressively increased after injection, reaching a maximum at 4 hours post-injection (Fig. 5B and 5C). This was followed by a gradual metabolic clearance, with a noticeable decrease in signal intensity at 16 hours. Notably, at the peak time point (4 h), the liver signal from the dicationic QMC-N-GGT

View Article Online DOI: 10.1039/D6SC02037B

was substantially stronger than that of its single positive charged QMC-C-GGT and zwitterionic QMC-SO_3-GGT (Fig. 5D). To ensure the reliability of this approach in complex internal environments, we validated the stability of the reference signal (Channel 1). As shown in Fig. S9, the fluorescence intensity of Channel 1 remained highly stable across a wide physiological pH range (pH 4.0–9.0), confirming its photophysical stability to local pH fluctuations. Furthermore, Zeta potential measurements (Fig. S10) revealed that QMC-N-GGT maintained a significantly positive charge (~12 mV) even after incubation with 50% FBS, indicating that the dicationic scaffold is not completely shielded by protein corona formation.This result strongly supports that the double positive charge strategy effectively promotes liver enrichment and retention.

In *Schistosoma*-infected mice, the activated form of QMC-N-GGT produced much stronger fluorescence in channel 2 (at the liver site), along with a weak signal in channel 1 (Fig. 5E). This could be attributed to the liver GGT-triggered activation. This response was significantly more pronounced with QMC-N-GGT than the other two probes, yielding the highest signal-to-noise ratio for detecting *Schistosoma*-infection (Fig. 5F and 5G). Biodistribution analysis of major organs collected 24 hours post-injection showed that all three probes were primarily localized in the liver, with weaker signals in the kidneys and negligible fluorescence in the heart, spleen, and lungs (Fig. 5H). Consistent with the real-time imaging data, QMC-N-GGT exhibited the highest hepatic fluorescence intensity both in channel 1 and 2 (in isolated liver, Fig. 5J and 5K), further supporting its superior liver-targeting and GGT-sensing capability. Histological examination (H&E staining) of organs from healthy mice treated with QMC-N-GGT revealed no apparent morphological damage or inflammatory infiltration compared to the PBS control group (Fig. S11), indicating good biocompatibility *in vivo*. All these *in vivo* results demonstrate that double positive charged QMC-N-GGT integrates excellent liver-targeting properties with the capacity for real-time, specific visualization of GGT upregulation. This enables intact diagnosis of *Schistosoma*-infection during its pathological progression, highlighting its potential as a precision imaging tool for staging *Schistosoma*-infection.

Intact tracking the spatio-temporal progression: staging *Schistosoma*-infection in living mice

The dual-channel response and hepatic targeting capability of QMC-N-GGT inspired us to further explore its utility for staged diagnosis of *Schistosoma*-infection progression. With this in mind, we systematically monitored the pathological progression of hepatic fibrosis induced by *Schistosoma japonicum* infection in a murine model (Fig. 6A). According to the experimental timeline, the infection progressed from initial percutaneous exposure on day 0 to severe pathology by day 40. To correlate the probe's fluorescence response with the actual physiological state, histopathological analysis was performed using H&E and Masson's trichrome staining.[55-57] The H&E sections revealed progressive hepatic structural disorganization and inflammatory infiltration (marked in Fig. 6B), while the Masson's trichrome staining clearly depicted the severity-dependent deposition of collagen (blue regions in Fig. 6C). These results confirmed the transition from a healthy liver to slight, middle, and severe infection states, thereby providing a robust biochemical basis for our GGT-responsive imaging using QMC-N-GGT.

Subsequently, *in vivo* fluorescence imaging was employed to track the real-time activation of the probe across varying infection stages (normal, slight, middle, and severe, Fig. 6D). Following intravenous administration of QMC-N-GGT, in the healthy group, no significant fluorescence enhancement (Channel 2) was observed, demonstrating the remarkably low background and excellent stability of QMC-N-GGT against non-specific activation. In contrast, infected mice showed a rapid and substantial signal increase at 800 nm, with the fluorescence intensity positively correlated with the infection severity.

Kinetic profiles further characterize the response of the probe toward varying levels of *Schistosoma*-infection. Although fluorescence increased continuously over 60 minutes in all groups, both the fluorescent response kinetics and intensity level differed markedly among severity stages (Fig. 6E and 6F). Specifically, the severe infection group displayed the fastest activation kinetics and the highest final signal. Quantitative analysis confirmed this severity-dependent trend: the average fluorescence intensity at the 60-minute time points increased stepwise from the slight to severe infection groups, with all infected stages showing a statistically significant enhancement ($p < 0.001$) compared to the normal control. Thus, QMC-N-GGT successfully transduces the pathological progression of *Schistosoma*-infection into a severity-dependent NIR signal with high spatiotemporal resolution. These results establish the probe as a powerful diagnostic tool for the *in situ* mapping and staging of schistosomiasis.

CONCLUSIONS

In summary, we have developed a rational molecular engineering strategy to address the critical bottleneck in non-invasive staging of *Schistosoma*-infection, which remains challenge for conventional anatomical imaging. Unlike traditional microscopic examination and ultrasonography diagnostic modalities limited by sensitivity or late stage detection, our approach focuses on the precise charge-regulation of a quinoline scaffold to optimize probes' *in vivo* pharmacokinetics for dual-channel ratiometric sensing. Specifically, by manipulating the fluorophore core from zwitterionic, single positive charge, to double positive charge, the optimized probe QMC-N-GGT achieves significant enhancement in hepatic accumulation via electrostatic recruitment to the anionic fibrotic microenvironment.

Leveraging this hepatotropic targeting and a GGT-activatable dual-channel ratiometric mechanism, QMC-N-GGT enables high-fidelity visualization of enzymatic dynamics with a remarkable signal-to-noise ratio. We established the mouse model of *Schistosoma*-infection via standard protocol. Crucially, the probe successfully decodes the spatiotemporal evolution of *Schistosoma*-infection, accurately differentiating slight, middle, and severe stages through distinct fluorescence kinetic profiles, a capability previously unattainable in real-time *in vivo* settings. This study not only provides a potent chemical tool for the precise evolution staging of parasitic diseases but also establishes a generalized paradigm for designing charge-regulated molecular probes to interrogate complex deep-tissue pathologies in clinical translation.

Data availability

Supporting data have been included in the article's ESI‡. All data generated and analyzed during the study are available from the corresponding authors on reasonable request.

Ethical Statement

All animal procedures were performed in accordance with the Guidelines for Care and Use of Laboratory Animals of East China University of Science and Technology (ECUST-2023-026) and approved by the Institutional Animal Care and Use Committee of National Tissue Engineering Center (Shanghai, China)

Author Contributions

All the experiments were conducted by X.M., E.X., Q.L., C.S., and Y.Y., with the supervision of C.Y., Q.L., W.Z., and Z.G.. All the authors analyzed the data and contributed to the manuscript writing.

Conflicts of interest

The authors declare no competing financial interest.

Acknowledgements

This work was supported by National Key Research and Development Program (2023YFA1802000), NSFC/China (22225805, 32121005, T2522013, 32394001, and 22378122), Shanghai Science and Technology Innovation Action Plan (No. 23J21901600), Innovation Program of Shanghai Municipal Education Commission, Shanghai Frontier Science Research Base of Optogenetic Techniques for Cell Metabolism (Shanghai Municipal Education Commission, grant 2021 Sci & Tech 0328), Science and Technology Commission of Shanghai Municipality (24DX1400200), and the Fundamental and Interdisciplinary Disciplines Breakthrough Plan of the Ministry of Education of China (JYB2025XDXM404).

Notes and references

(1) Gryseels, B.; Polman, K.; Clerinx, J.; Kestens, L., Human schistosomiasis. *Lancet* **2006**, *368* (9541), 1106-18.

(2) Houlder, E. L.; Stam, K. A.; Koopman, J. P. R.; König, M. H.; Langenberg, M. C. C.; Hoogerwerf, M. A.; Niewold, P.; Sonnet, F.; Janse, J. J.; Partal, M. C.; Sijtsma, J. C.; de Bes-Roeleveld, L. H. M.; Kruize, Y. C. M.; Yazdanbakhsh, M.; Roestenberg, M., Early symptom-associated inflammatory responses shift to type 2 responses in controlled human schistosome infection. *Sci. Immunol.*, **2024**, *9* (97), eadl1965.

(3) You, Y.; Cheng, S.; Chen, X.; Chen, X.; Yi, C.; Cai, M.; Luo, F.; Wang, X.; Xie, Y.; Yang, W.; Xiu, L.; Gu, M.; Sun, C.; Huo, L.; Chen, G.; Li, S.; Wang, J.; Hu, W., Dynamic single-cell transcriptomics *reveals lsamp-guided neural network formation in male S.* japonicum driving female reproduction. *Nat. Commun.*, **2026**, *17* (1), 1602.

(4) Lo, N. C.; Bezerra, F. S. M.; Colley, D. G.; Fleming, F. M.; Homeida, M.; Kabatereine, N.; Kabole, F. M.; King, C. H.; Mafe, M. A.; Midzi, N.; Mutapi, F.; Mwanga, J. R.; Ramzy, R. M. R.; Satrija, F.; Stothard, J. R.; Traoré, M. S.; Webster, J. P.; Utzinger, J.; Zhou, X. N.; Danso-Appiah, A.; Eusebi, P.; Loker, E. S.; Obonyo, C. O.; Quansah, R.; Liang, S.; Vaillant, M.; Murad, M. H.; Hagan, P.; Garba, A., Review of 2022 WHO guidelines on the control and elimination of schistosomiasis. *Lancet Infect. Dis.*, **2022**, *22* (11), e327-e335.

(5) Langenberg, M. C. C.; Hoogerwerf, M. A.; Koopman, J. P. R.; Janse, J. J.; Kos-van Oosterhoud, J.; Feijt, C.; Jochems, S. P.; de Dood, C. J.; van Schuijlenburg, R.; Ozir-Fazalalikhan, A.; Manurung, M. D.; Sartono, E.; van der Beek, M. T.; Winkel, B. M. F.; Verbeek-Menken, P. H.; Stam, K. A.; van Leeuwen, F. W. B.; Meij, P.; van Diepen, A.; van Lieshout, L.; van Dam, G. J.; Corstjens, P.; Hokke, C. H.; Yazdanbakhsh, M.; Visser, L. G.; Roestenberg, M., A controlled human Schistosoma mansoni infection model to advance novel drugs, vaccines and diagnostics. *Nat. Med.*, **2020**, *26* (3), 326-332.

(6) Koopman, J. P. R.; Houlder, E. L.; Janse, J. J.; Lamers, O. A.; Roozen, G. V.; Sijtsma, J. C.; Casacuberta-Partal, M.; Hilt, S. T.; van der Stoep, M.; van Amerongen-Westra, I. M.; Brienen, E. A.; Wammes, L. J.; van Lieshout, L.; van Dam, G. J.; Corstjens, P. L.; van Diepen, A.; Yazdanbakhsh, M.; Hokke, C. H.; Roestenberg, M., Clinical tolerance but no protective efficacy in a placebo-controlled trial of repeated controlled schistosome infection. *J. Clin. Invest*., **2024**, *135* (4).

(7) Rivera, J.; Mu, Y.; Gordon, C. A.; Jones, M. K.; Cheng, G.; Cai, P., Current and upcoming point-of-care diagnostics for schistosomiasis. *Trends. Parasitol*., **2024**, *40* (1), 60-74.

(8) Berger, D. J.; Crellen, T.; Lamberton, P. H. L.; Allan, F.; Tracey, A.; Noonan, J. D.; Kabatereine, N. B.; Tukahebwa, E. M.; Adriko, M.; Holroyd, N.; Webster, J. P.; Berriman, M.; Cotton, J. A., Whole-genome sequencing of Schistosoma mansoni reveals extensive diversity with limited selection despite mass drug administration. *Nat. Commun.*, **2021**, *12* (1), 4776.

(9) Zhang, B.; Lu, J.; Lin, X.; Wang, J.; Li, Q.; Jin, T.; Shi, Q.; Lu, Y.; Zhang, J.; Deng, J.; Zhang, Y.; Guo, Y.; Gao, J.; Chen, H.; Yan, Y.; Wu, J.; Gao, J.; Che, J.; Dong, X.; Gu, Z.; Lin, N., Injectable and sprayable fluorescent nanoprobe for rapid real-time detection of human colorectal tumors. *Adv. Mater.*, **2024**, *36* (36), e2405275.

(10) Li, H.; Kim, D.; Yao, Q.; Ge, H.; Chung, J.; Fan, J.; Wang, J.; Peng, X.; Yoon, J., Activity-based NIR enzyme fluorescent probes for the diagnosis of tumors and image-guided surgery. *Angew. Chem. Int. Ed*., **2021**, *60* (32), 17268-17289.

(11) Wang, X.; Ding, Q.; Groleau, R. R.; Wu, L.; Mao, Y.; Che, F.; Kotova, O.; Scanlan, E. M.; Lewis, S. E.; Li, P.; Tang, B.; James, T. D.; Gunnlaugsson, T., Fluorescent probes for disease diagnosis. *Chem. Rev*., **2024**, *124* (11), 7106-7164.

(12) Cao, S.; Sun, C.; Zhang, X. Y.; Yoon, C.; Liu, Z.; Yoo, J.; Kim, Y.; Yu, X.; Xu, Y.; Kim, J. S.; Wang, K. N., Real-time super-resolution tracking of mtDNA remodeling and inflammatory release with a selective fluorescent probe. *Angew. Chem. Int. Ed.*, **2026**, *65* (7), e20934.

(13) Fujita, K.; Kamiya, M.; Yoshioka, T.; Ogasawara, A.; Hino, R.; Kojima, R.; Ueo, H.; Urano, Y., Rapid and accurate visualization

of breast tumors with a fluorescent probe targeting α-mannosidase 2C1. *ACS Central Sci*., **2020**, *6* (12), 2217-2227.

(14) Han, J.; Yang, M.; Lv, C.; Li, K.; Fan, J.; Peng, X., A unimolecular near-infrared fluorescent probe for in vivo imaging of enzymes with minimized false-negative signals. *Chem. Sci.*, **2026**, *17* (5), 2791-2801.

(15) Wu, L.; Li, Z.; Wang, K.; Groleau, R. R.; Rong, X.; Liu, X.; Liu, C.; Lewis, S. E.; Zhu, B.; James, T. D., Advances in organic small molecule-based fluorescent probes for precision detection of liver diseases: a perspective on emerging trends and challenges. *J. Am. Chem. Soc.*, **2025**, *147* (11), 9001-9018.

(16) Mao, Y.; Zhang, W.; Wang, X.; Li, P.; Tang, B., Rational design of fluorescent imaging agents for hepatic diseases: from molecular mechanisms to diagnostic precision. *Chem. Soc. Rev.*, **2026**, 10.1039/d5cs00947b.

(17) Xia, T.; Xia, Z.; Tang, P.; Fan, J.; Peng, X., Light-driven mitochondrion-to-nucleus DNA cascade fluorescence imaging and enhanced cancer cell photoablation. *J. Am. Chem. Soc.*, **2024**, *146* (19), 12941-12949.

(18) Wu, X.; Xing, F.; Yang, Y.; Liu, X.; Kim, G.; Jiang, Q.; Xu, Y.; Hu, J. J.; Liang, G.; Yoon, J., Caged ligand-decorated near-infrared photosensitizer with in vivo albumin-hijacking capacity for tumor-targeted hypoxia-tolerant photoimmunotherapy of cancer. *J. Am. Chem. Soc.*, **2026**, *148* (6), 6135-6147.

(19) Tang, Y.; Li, Y.; He, C.; Wang, Z.; Huang, W.; Fan, Q.; Liu, B., NIR-II-excited off-on-off fluorescent nanoprobes for sensitive molecular imaging in vivo. *Nat. Commun.*, **2025**, *16* (1), 278.

(20) Wang, H.; Zhang, X.; Li, P.; Huang, F.; Xiu, T.; Wang, H.; Zhang, W.; Zhang, W.; Tang, B., Prediction of early atherosclerotic plaques using a sequence-activated fluorescence probe for the simultaneous detection of γ-glutamyl transpeptidase and hypobromous acid. *Angew. Chem. Int. Ed.*, **2024**, *63* (1), e202315861.

(21) An, R.; Wei, S.; Huang, Z.; Liu, F.; Ye, D., An activatable chemiluminescent probe for sensitive detection of γ-glutamyl transpeptidase activity in vivo. *Anal. Chem*., **2019**, *91* (21), 13639-13646.

(22) Wang, S.; Lian, D.; Sun, C.; Xu, M.; Zhu, M.; Yan, C.; Guo, Z., High selective NIR-II fluorescent probe for sensing phosgene in plants. *Chinese Chem. Lett.*, **2025**. 10.1016/j.cclet.2025.111744

(23) Dai, B.; Huang, S.; Hu, Q.; Wang, P.; Gong, L.; Xu, G.; Wu, F.; Qin, H.; Xia, S.; Sun, W.; Li, H.; Feng, Z.; Ren, C.; Shen, J.; Liu, M., Circular RNA Gsr-0002 promotes schistosomiasis-induced liver fibrosis by regulating the DNMT3A/PTEN pathway. *Int. J. Biol. Macromol.* **2025**, *333* (Pt 1), 148776.

(24) He, X.; Sun, Y.; Lei, N.; Fan, X.; Zhang, C.; Wang, Y.; Zheng, K.; Zhang, D.; Pan, W., MicroRNA-351 promotes schistosomiasis-induced hepatic fibrosis by targeting the vitamin D receptor. *Proc. Natl. Acad. Sci. U. S. A.*, **2018,** *115* (1), 180-185.

(25) Li, K.; Lyu, Y.; Huang, Y.; Xu, S.; Liu, H. W.; Chen, L.; Ren, T. B.; Xiong, M.; Huan, S.; Yuan, L.; Zhang, X. B.; Tan, W., A de novo strategy to develop NIR precipitating fluorochrome for long-term in situ cell membrane bioimaging. *Proc. Natl. Acad. Sci. U. S. A*., **2021**, *118* (8), e2018033118.

(26) Wang, H.; Zhang, X.; Li, P.; Huang, F.; Xiu, T.; Wang, H.; Zhang, W.; Zhang, W.; Tang, B., Prediction of early atherosclerotic plaques using a sequence-activated fluorescence probe for the simultaneous detection of γ-glutamyl transpeptidase and hypobromous acid. *Angew. Chem. Int. Ed.*, **2024**, *63* (1), e202315861.

(27) Zhao, M.; Lu, Y.; Zhang, Y.; Xue, H.; Guo, Z., Ultra-high signal-to-noise ratio near-infrared chemiluminescent probe for *in vivo* sensing singlet oxygen. *Chinese Chem. Lett.*, **2025,** *36* (5).

(28) Bian, H.; Ma, D.; Pan, F.; Zhang, X.; Xin, K.; Zhang, X.; Yang, Y.; Peng, X.; Xiao, Y., Cardiolipin-targeted NIR-II fluorophore causes "avalanche effects" for re-engaging cancer apoptosis and inhibiting metastasis. *J. Am. Chem. Soc.*, **2022**, *144* (49), 22562-22573.

(29) Chen, L.; He, Y.; Lan, J.; Li, Z.; Gu, D.; Nie, W.; Zhang, T.; Ding, Y., Advancements in nano drug delivery system for liver cancer therapy based on mitochondria-targeting. *Biomed. Pharmacother*., **2024**, *180*, 117520.

(30) Chang, M.; Yan, C.; Shi, L.; Li, D.; Fu, W.; Guo, Z., Rational design of shortwave infrared (SWIR) fluorescence probe: Cooperation of ICT and ESIPT processes for sensing endogenous cysteine. *Chinese Chem. Lett.*, **2022,** *33* (2), 762-766.

(31) Zhang, D.; Teng, K. X.; Shao, N.; Niu, L. Y.; Yang, Q. Z., Cascade responsive photosensitizer for precise delivery and photodynamic therapy. *J. Med. Chem*., **2025**, *68* (8), 8648-8658.

(32) Zhang, X.; Shen, S.; Liu, D.; Li, X.; Shi, W.; Ma, H., Combination of changeable π-conjugation and hydrophilic groups for developing water-soluble small-molecule NIR-II fluorogenic probes. *Chem. Sci.*, **2023**, *14* (11), 2928-2934.

(33) Li, N.; Liu, Z.; Chen, C.; Jiang, H.; Liu, Y.; Ni, D., Activatable fluorescent ratiometric probes for early diagnosis and prognostic assessment of acute kidney injury. *Sci. Adv*., **2025**, *11* (43), eaea1654.

(34) Zhang, Y.; Chen, X.; Yuan, Q.; Bian, Y.; Li, M.; Wang, Y.; Gao, X.; Su, D., Enzyme-activated near-infrared fluorogenic probe with high-efficiency intrahepatic targeting ability for visualization of drug-induced liver injury. *Chem. Sci.*, **2021**, *12* (44), 14855-14862.

(35) Zhou, Q.; Shao, S.; Wang, J.; Xu, C.; Xiang, J.; Piao, Y.; Zhou, Z.; Yu, Q.; Tang, J.; Liu, X.; Gan, Z.; Mo, R.; Gu, Z.; Shen, Y., Enzyme-activatable polymer-drug conjugate augments tumour penetration and treatment efficacy. *Nat. Nanotechnol*., **2019**, *14* (8), 799-809.

(36) Ye, Z.; Qiu, C.; Liu, Z.; Wen, H.; Gao, F.; Zhang, Y.; Wang, W. J.; Zhang, J.; Qiu, Z.; Zhang, W.; Alam, P.; Zhao, Z.; Tang, B. Z., Counterion-driven long-term imaging of cell membranes and migrasomes using dicationic NIR AIEgens. *J. Am. Chem. Soc.*, **2025**, *147* (31), 28442-28453.

(37) Miao, J.; Huo, Y.; Yao, G.; Feng, Y.; Weng, J.; Zhao, W.; Guo, W., Heavy atom-free, mitochondria-targeted, and activatable photosensitizers for photodynamic therapy with real-time in-situ therapeutic monitoring. *Angew. Chem. Int. Ed.*, **2022**, *61* (25), e202201815.

(38) Zuo, J.; Peng, A.; Wu, P.; Chen, J.; Yao, C.; Pan, J.; Zhu, E.; Weng, Y.; Zhang, K.; Feng, H.; Jin, Z.; Qian, Z., Charge-regulated fluorescent anchors enable high-fidelity tracking of plasma membrane dynamics during biological events. *Chem. Sci.*, **2024**, *15* (23), 8934-8945.

(39) Zhang, J.; Hu, Y.; Wen, X.; Yang, Z.; Wang, Z.; Feng, Z.; Bai, H.; Xue, Q.; Miao, Y.; Tian, T.; Zheng, P.; Zhang, J.; Li, J.; Qiu, L.; Xu, J. J.; Ye, D., Tandem-controlled lysosomal assembly of nanofibres induces pyroptosis for cancer immunotherapy. *Nat. Nanotechnol*., **2025**, *20* (4), 563-574.

(40) Radmand, A.; Kim, H.; Beyersdorf, J.; Dobrowolski, C. N.; Zenhausern, R.; Paunovska, K.; Huayamares, S. G.; Hua, X.; Han, K.; Loughrey, D.; Hatit, M. Z. C.; Del Cid, A.; Ni, H.; Shajii, A.; Li, A.; Muralidharan, A.; Peck, H. E.; Tiegreen, K. E.; Jia, S.; Santangelo, P. J.; Dahlman, J. E., Cationic cholesterol-dependent LNP delivery to lung stem cells, the liver, and heart. *Proc. Natl. Acad. Sci. U. S. A*., **2024**, *121* (11), e2307801120.

(41) Yan, C.; Liu, C.; Liu, B.; Zheng, Q.; Zhao, X.; Lu, S.; Fu, X.; Li, W.; Li, J.; Li, D.; Yao, Y.; Zhang, Y.; Zhu, H.; Shi, P.; Zhu, W. H.; Guo, Z., Fluorescence lifetime clocks quantify senescence and aging. *Nat. Aging*, **2025**, *5* (12), 2532-2545.

(42) Yao, Y.; Chen, J.; Yan, C.; Gao, M.; Liu, J.; Zhu, W. H.; Fan, C.; Guo, Z., Excitation-matchable shortwave infrared quinolinium fluorophores: decoding spatiotemporal interactions with multiplexed bioimaging. *J. Am. Chem. Soc.*, **2025**, *147* (51), 46953-46965.

(43) Liu, Q.; Li, Z.; Huang, Y.; Lin, Z.; Shen, X. C.; Chen, H., Deep-NIR to NIR-II hemicyanine fluorophore scaffolds with dual optically tunable sites for *in vivo* multiplexed imaging. *Chem. Sci.*, **2025,** *16* (48), 23394-23404.

(44) Yang, H.; Li, D.; Wu, J.; Pu, K., Shortwave infrared hemicyanine-6 for cancer-activated and shaving-free preclinical imaging of lung metastasis. *J. Am. Chem. Soc.*, **2025,** *147* (34), 30794-30802.

(45) Fan, W.; Adebowale, K.; Vancza, L.; Li, Y.; Rabbi, M. F.; Kunimoto, K.; Chen, D.; Mozes, G.; Chiu, D. K.; Li, Y.; Tao, J.; Wei, Y.; Adeniji, N.; Brunsing, R. L.; Dhanasekaran, R.; Singhi, A.; Geller, D.; Lo, S. H.; Hodgson, L.; Engleman, E. G.; Charville, G. W.; Charu, V.; Monga, S. P.; Kim, T.; Wells, R. G.; Chaudhuri, O.; Torok, N. J., Matrix viscoelasticity promotes liver cancer progression in the pre-cirrhotic liver. *Nature*, **2024**, *626* (7999), 635-642.

(46) Nicoli, A. M.; Frei, M. S., Synthetic fluorophores for live-cell fluorescence microscopy and biosensing. *Nat. Chem. Biol*., **2025**, *21* (12), 1846-1858.

(47) Wang, X.; Liew, S. S.; Huang, J.; Hu, Y.; Wei, X.; Pu, K., Dual-locked enzyme-activatable bioorthogonal fluorescence turn-on imaging of senescent cancer cells. *J. Am. Chem. Soc.*, **2024**, *146* (32), 22689-22698.

(48) Ma, Y.; Yan, C.; Guo, Z.; Tan, G.; Niu, D.; Li, Y.; Zhu, W. H., Spatio-temporally reporting dose-dependent chemotherapy via uniting dual-modal MRI/NIR imaging. *Angew. Chem. Int. Ed.*, **2020**, *59* (47), 21143-21150.

(49) Yan, C.; Guo, Z.; Liu, Y.; Shi, P.; Tian, H.; Zhu, W. H., A sequence-activated and logic dual-channel fluorescent probe for tracking programmable drug release. *Chem. Sci.*, **2018**, *9* (29), 6176-6182.

(50) Meng, H.; Wang, J.; Wen, H.; Xu, Z.; Luo, L.; Lin, W.; Lu, K.; Lu, Y.; Wang, J.; Xiong, Y.; Xu, J.; Mao, Z. W.; Xia, W., Evoking simultaneous ferroptosis and apoptosis by a dual-locked platinum (IV) prodrug for synergistic chemo-immunotherapy. *Angew. Chem. Int. Ed.*, **2025**, *64* (28), e202505930.

(51) Chu, F.; Feng, B.; Zhou, Y.; Liu, M.; Zhang, H.; Liu, M.; Chen, Q.; Zhang, S.; Ma, Y.; Dong, J.; Chen, F.; Zeng, W., Debut of enzyme-responsive anionic cyanine for overlap-free NIR-II-to-I dual-channel tumour imaging. *Chem. Sci.*, **2025**, *16* (10), 4490-4500.

(52) Liu, W.; Huang, B.; Tong, Z.-X.; Wang, S.; Li, Y.-J.; Dai, Y.-Y., A sensitive two-photon ratiometric fluorescent probe for γ-glutamyltranspeptidase activity detection and imaging in living cells and cancer tissues. *New J. Chem.*, **2018**, *42* (7), 5403-5407.

(53) Hino, H.; Kamiya, M.; Kitano, K.; Mizuno, K.; Tanaka, S.; Nishiyama, N.; Kataoka, K.; Urano, Y.; Nakajima, J., Rapid Cancer Fluorescence Imaging Using A γ-glutamyltranspeptidase-specific probe for primary lung cancer. *Transl. Oncol*., **2016**, *9* (3), 203-210.

(54) Wu, Q.; O'Connor, H. M.; Elston, D. M., Retrospective analysis of Verhoeff-Van Gieson elastic staining, diffractive microscopy, and Masson trichrome staining in the diagnosis of alopecia. *J. Am. Acad. Dermatol*., **2020**, *82* (1), 247-249.

(55) West, K. L.; Proia, A. D.; Puri, P. K., Fontana-Masson stain in fungal infections. *J. Am. Acad. Dermatol*., **2017**, *77* (6), 1119-1125.

(56) Pan, J.; Xiong, W.; Zhang, A.; Zhang, H.; Lin, H.; Gao, L.; Ke, J.; Huang, S.; Zhang, J.; Gu, J.; Chang, A. C. Y.; Wang, C., The imbalance of p53-park7 signaling axis induces iron homeostasis dysfunction in doxorubicin-challenged cardiomyocytes. *Adv. Sci*., **2023**, *10* (15), e2206007.

(57) Wei, F. L.; Zhai, Y.; Wang, T. F.; Zhao, J. W.; Wang, C. L.; Tang, Z.; Shen, K.; Wu, H.; Zheng, R.; Du, M. R.; Heng, W.; Li, X. X.; Yan, X. D.; Gao, Q. Y.; Guo, Z.; Qian, J. X.; Zhou, C. P., Stem cell-homing biomimetic hydrogel promotes the repair of osteoporotic bone defects through osteogenic and angiogenic coupling. *Sci. Adv.*, **2024**, *10* (44), eadq6700.

View Article Online
DOI: 10.1039/D5SC02037B

View Article Online
DOI: 10.1039/D6SC02037B

Supporting data have been included in the article's ESI‡. All data generated and analyzed during the study are available from the corresponding authors on reasonable request.